Ultramicroscopy 215 (2020) 113022

Contents lists available at ScienceDirect

Ultramicroscopy

journal homepage: www.elsevier.com/locate/ultramic

Vector Potential Photoelectron Microscopy Instrument Design

R. Browning*

R. Browning Consultants, 1 Barnhart Place, Shoreham, NY 11786

A B S T R A C T

This report covers the main aspects of designing a vector potential photoelectron microscope (VPPEM). While the VPPEM is straightforward in concept, there are several areas where the optimum configuration of the optics is not immediately obvious, and compromises must be made to make a practical instrument. This report summarizes our instrumental setups, and some basic design issues.

1. Introduction

Vector potential photoelectron microscopy (VPPEM) is a new technique for materials microanalysis at the meso scale [1-3]. VPPEM images the elemental and chemical makeup of the top few nanometers of a sample using near edge x-ray absorption fine structure (NEXAFS) as the main image contrast mechanism. VPPEM will be able to image many types of samples including: samples with rough or contoured surfaces, poor conductors, or even poorly consolidated samples such as powder residues. The source of x-rays needs to be a bright tunable x-ray source such as a synchrotron beam line. This report concentrates on main aspects of the design which are seen as necessary to produce a practical instrument.

The VPPEM optical system needs some introduction. The optical system is a new class of imaging system, it has no analog in any other imaging system either in light optics or electron optics. VPPEM uses the canonical momentum of the photoelectrons emitted into magnetic field to form an image. The canonical momentum of an electron in a magnetic field is [4]:

$$\boldsymbol{p} = m\dot{\boldsymbol{r}} + q\mathbf{A}(\mathbf{r}) \tag{1}$$

Where **p** is the momentum, $\dot{\boldsymbol{r}}$ the velocity, **A** is the vector potential, and m and q are the mass and charge of the photoelectron. Where, from Maxwell's equations, we have the magnetic field is the curl of the vector potential, $\mathbf{B} = \nabla \times \mathbf{A}$.

For a solenoid consisting of a circular loop of current **I** of radius R:

$$\mathbf{A}(r) = \frac{\mu_0}{4R} r\boldsymbol{I} \tag{2}$$

The direction of **A** is around the axis in the direction of the current. This is illustrated in Figure 1 where the arrows indicate the direction, and magnitude of the vector field. The vector potential field is radially symmetric, zero on the axis, and increases linearly with radius out to the loop radius. This distribution is a two-dimensional vector field each point defined by a unique direction and magnitude mapped onto a two dimensional space in angle θ around the axis, and radius r away from the axis,

Photoelectrons emitted into the vacuum from a sample surface inside a solenoid have an additional momentum due to their position in the vector potential field. It is this additional two-dimensional distribution of momentum that is projected through the electron optical system to form an image.

In producing an image, the VPPEM electron optical system is required to convert a wide energy range two-dimensional photoelectron momentum distribution into a monochromatic distribution projected onto a two-dimensional image plane. The VPPEM system has three main electron optical elements to achieve this: a magnetic enclosure, an electron energy analyzer, and focusing optics.

The magnetic enclosure comprises a solenoid magnet enclosed in a ferromagnetic shield with an aperture on the axis for the photoelectrons to exit the magnetic field. The energy analyzer is a concentric hemispherical analyzer (CHA). The focusing optics comprises two parts, one a condensing lens into the CHA, and the other a focusing lens out of the CHA to form a real mage on a detector. A schematic of the overall electron optical system is shown in Figure 2.

The novel part of the VPPEM optics is the action of the magnetic field in producing an angular image. The photoelectrons leave the sample at the center of the magnetic field along cyclotron orbits approximately parallel to the optical axis following the magnetic field lines. The maximum size of the cyclotron orbits depends on the energy of the photoelectrons. As the photoelectrons move towards a weaker field, the cyclotron orbits start to unwind, and become more collimated. The cyclotron orbits also start to move away from the axis as the trajectories follow down the expanding field lines. When the photoelectrons reach the aperture, there is a sudden change of the vector

* Corresponding author at: R. Browning Consultants, 1 Barnhart Pl, Shoreham, NY 11786, United States.
E-mail address: ray@rbrowning.net.

https://doi.org/10.1016/j.ultramic.2020.113022
Received 29 March 2020; Received in revised form 3 May 2020; Accepted 7 May 2020
Available online 26 May 2020
0304-3991/

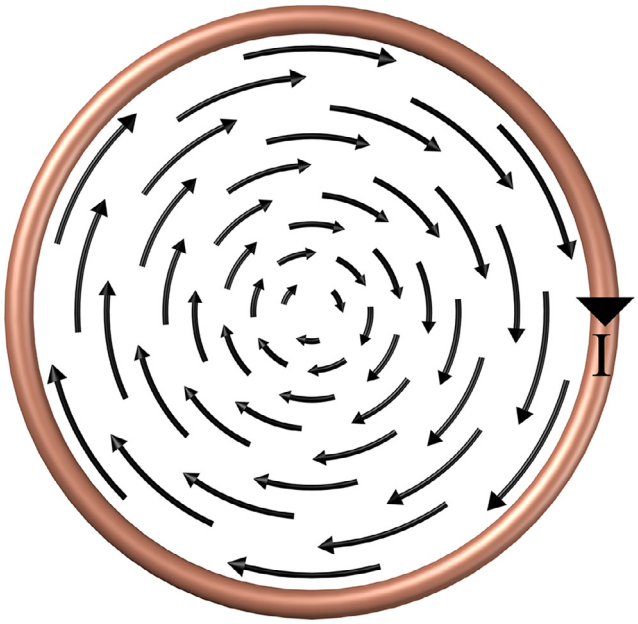

Figure 1. Arrows illustrate the magnitude and direction of the vector potential from a loop of current.

potential. This change of momentum leads to a force which deflects the electrons producing a two-dimensional angular image that is mapped to the angle and magnitude of the vector potential at the sample. (see Supplemental file 1 for further details of the deflection action, and Section 7 for a discussion of the electron optical consequences of having an angular image).

This angular image has a full spectrum of energies. The angular image is focused into the CHA using an electrostatic condenser lens. A CHA is double focusing in both angular directions, and a monochromatic angular image passes through the energy defining exit slit of the CHA. This monochromatic angular image is projected as a real image onto a microchannel plate electron image detector.

A cutaway illustration of a simple magnetic circuit with a numerical simulation of the action of the aperture on electron trajectories is shown in Figures 3 and 4.

In the simulation of Figure 4 the fan of trajectories leaving the magnetic field have started at different off-axis positions at the sample position: ± 10, 20, 30, 40, and 50 microns. The central field is 0.2 Tesla, the ferromagnet shield is a cylindrical box of 100 mm radius, the aperture is 4 mm diameter, and the trajectories are simulations for 50 eV electron energies. The trajectory plot of Figure 4 is deceptively simple, only the radial distance of the trajectories from the axis is plotted. In fact, the image is rotated around the axis, and it is not a simple angular image.

Figure 5 shows a simulated trajectory of a 500 eV electron from a 1.0 Tesla field emitted at 45° to the magnetic axis, and at a small distance off-axis in the x direction. In Figure 5 we are looking down the magnetic axis. We see the cyclotron orbit move away from the y axis, and expand as the field decreases. As the trajectory exits the field, it undergoes a deflection into its final direction. Clearly, the final direction will depend on exactly where the orbit crosses the aperture as the vector potential varies across the aperture. Two things to note about the final direction of the trajectory. Firstly, it is aligned at an angle to the x,y axis, and secondly it does not cross the x, and y axis in the same place. This is what we expect as the vector potential is pointing around the axis, and the starting position of the cyclotron orbit is off axis. The orbit moves further off-axis as magnetic field weakens. If we plot the trajectories in the x, and y directions separately, Figure 6, we see the image is rotated, and that the image has its apparent origin on the optical axis in different positions on the x (the meridional) and the y (the transverse) directions.

The different apparent object positions is a complication when it comes to focusing the image out of the VPPEM aperture into the CHA. In fact, the input lens could be viewed as a condenser because a true focus is not obtainable.

In the VPPEM, electrons of all energies from a sample are deflected into an angular image by the change in vector potential at the aperture. This angular image has to be converted into a monochromatic real image focused at an image plane. Figure. 2 illustrates the electrostatic elements needed. Diverging electron trajectories exiting the VPPEM aperture are focused into a concentric hemispherical analyzer (CHA) by a multielement cylindrical electrostatic lens. After energy analysis by the CHA, which is double focusing, the angular monochromatic image is projected as a real image onto an image detector using a second cylindrical electrostatic lens.

As shown in Figure 2 the CHA is operated without an input slit, but with an energy defining output slit. This is the reverse of the normal operation for a CHA. The utility of this arrangement is that with no input slit blocking the line of sight, the photon beam can enter the instrument through the alignment port at the back of the CHA, pass down the axis of the instrument, and illuminate the sample at normal incidence.

If we run the simulation of Figure 5 with a range of off axis angles from 0° to 90°, and with a weighting for a cosine emission distribution, we would expect to get a cone of confusion equivalent to the disk of confusion from a magnetic projection microscope [5]. This is what we find. By ray tracing over the full range of angles, we can see the VPPEM angular cone of confusion is caused by the variation of the exit point in the vector potential field at the aperture.

The calculated VPPEM spatial resolution is dependent on the cyclotron radius of the photoelectrons at the sample. The cyclotron radius at the sample depends on the magnetic field, and the imaged electron energy. A good approximation for the 20-80% edge spatial resolution ρ in microns is:

$$\rho = 3\frac{\sqrt{E}}{B} \tag{3}$$

Where E is the electron energy in electron volts, and B the magnetic field in Tesla [6]. A useful feature of the strong magnetic field containment of the emitted electrons is that they can be accelerated, or decelerated within the magnetic field without distorting the image. Very low energy electrons, with energies below 1eV, can be imaged by accelerating them off the sample to several tens of electron volts. It has been our practice to collect NEXAFS spectra with different low energy take-off energies to maximize spatial resolution. Interestingly, the spatial resolution at compositional interfaces appears to be greater than expected. One possible explanation is the surface fields from chemical inhomogeneities are influencing the electron trajectories[2].

The VPPEM electron optical path is unusual for a microscope in that the sample, and the image are not on conjugate planes. Although there is a one to one mapping of points from the sample to the image, the sample is not sitting at a particular plane in the electron optics, and the virtual image of the sample is at the field termination aperture. The sample itself is sitting in the center of a cylinder formed by the vector potential field distribution. If the vector potential field is constant over a distance near the center of the solenoid axis, then the sample will be imaged at the same magnification within this distance. It will not go out of 'focus', the effective depth of field can be relatively large.

This introduction gives an outline of the electron optics of VPPEM. There are clearly some complications in how the image is formed, and this impacts the actual design and implementation of a VPPEM system. The design of the optical system must be done as a whole because design of the different parts impact each of the others. However, it is useful to begin by discussing the different sections separately.

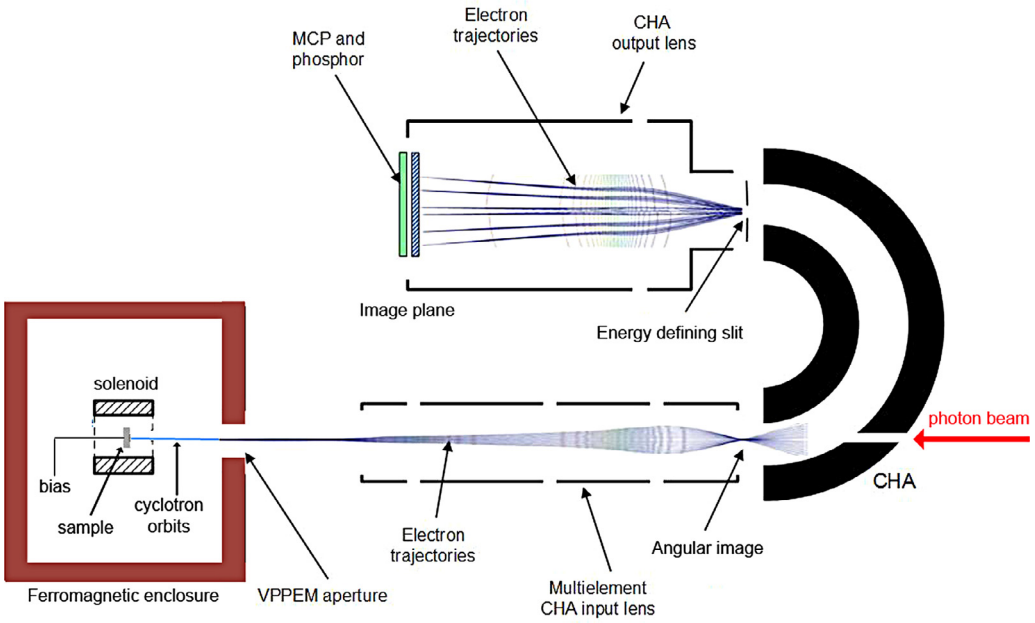

Figure 2. Schematic of the electron optical elements comprising a VPPEM.

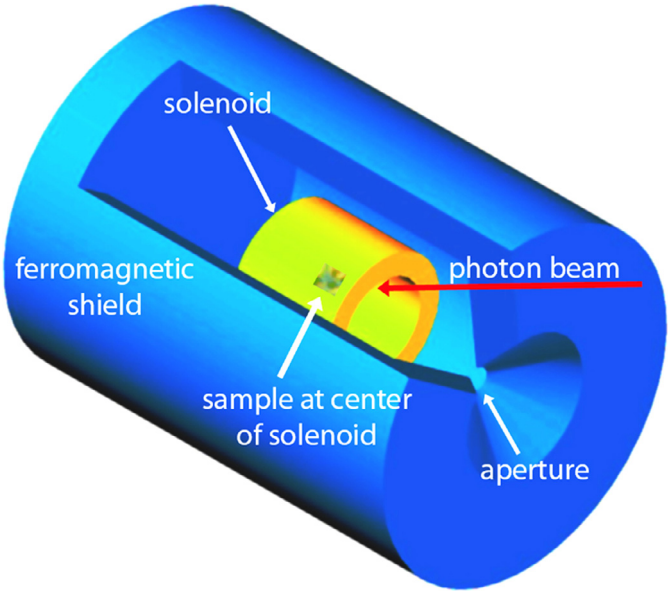

Figure 3. Cutaway of a simple VPPEM magnetic circuit.

2. The magnetic circuit

The magnetic circuit is the core part of the VPPEM. It is composed of a solenoid magnet surrounded by a ferromagnetic enclosure with an aperture along the axial direction of the solenoid. There are a wide range of possible magnetic solutions. The geometric arrangement with the photon beam path entering through the back of the CHA along the optic axis means that the magnet has few restrictions on its design. There is also flexibility in how we construct the magnetic circuit.

We have two extreme cases in the magnetic design. The first is to have the magnet essentially independent of the enclosure, so that the enclosure just acts as a magnetic shield, with a minimum of interaction, and force, between the solenoid and the shield. This arrangement may also include field cancelling coils enabling a strong central field with weak external fields. The other extreme is to make the ferromagnetic enclosure part of the magnet, in effect an electromagnet yoke, with a strong coupling between the solenoid field and the ferromagnetic shield.

While it will depend on the experimental circumstances, it is the case that the working volume of the microscope will be small. Therefore it seems more appropriate to look for magnetic solutions with relatively compact magnets. A small magnetic volume is safer, more easily shielded, and easier to fit in to the geometry of the instrument. Compact electromagnetic yoke solutions using high temperature superconducting (HTS) tapes are available commercially up to nearly 20 Tesla so these might be the most straightforward choices.

The magnetic field is used to form and manipulate the image in several ways. First, there is the action of the sudden magnetic field termination to form the initial angular image. Second, we use the exit magnet field design to change the angular magnification which can be expressed as radians per micron. By allowing the electrons trajectories to pass from the strong central field to the ferromagnetic aperture at a weaker field, we reduce the final magnitude of the vector potential. This reduces the off-axis momentum at the aperture which determines the angular magnification. Third, we make use of the magnetic field to change the energy of the photoelectrons. The strong containment of the electron trajectories in cyclotron obits around the magnetic field line means we can accelerate or decelerate the photoelectrons by biasing the sample without introducing distortion in the image. We can control the angular magnification this way by changing the electron forward momentum, and we can easily select which emitted electron energies we finally image by changing the sample bias.

We need to set multiple parameters in the optical design of the magnetic circuit. These are the strength of the central magnetic field, the ratio of initial magnetic field to the field at the termination, the final field strength at termination, and the energy of the electrons at the termination. We also want to understand what the choice of the shape, size, and magnetic properties of the field termination will do to the image. The termination will be in very different environments depending on the final field, and this is a very non-linear.

Having several parameters that can be freely changed implies a large multidimensional design space. It would be good to generate some rules of thumb to guide the design process. However, because the system is very non-linear this is not as straightforward as it might seem. Example calculations of the field termination with different design parameters are presented in Supplemental file 2. These calculations show that there are no easy answers to the design questions. In general,

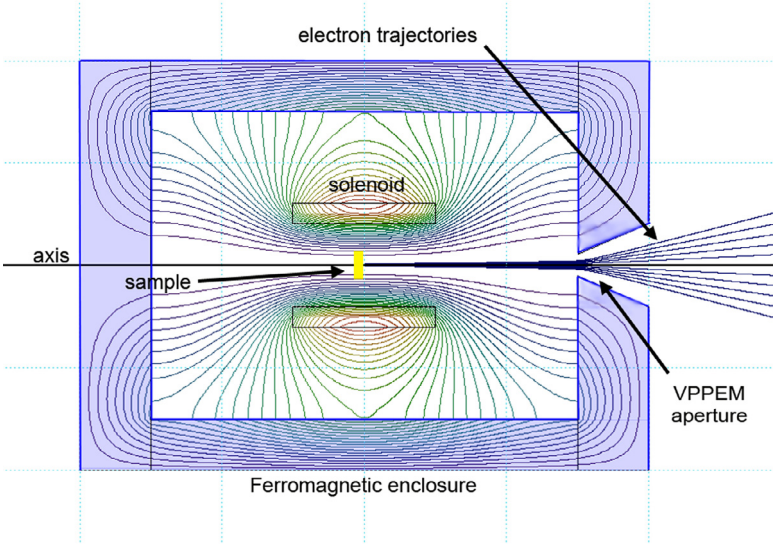

Figure 4. Numerical simulation of the magnetic field and electron trajectories for a cylindrical magnetic enclosure.

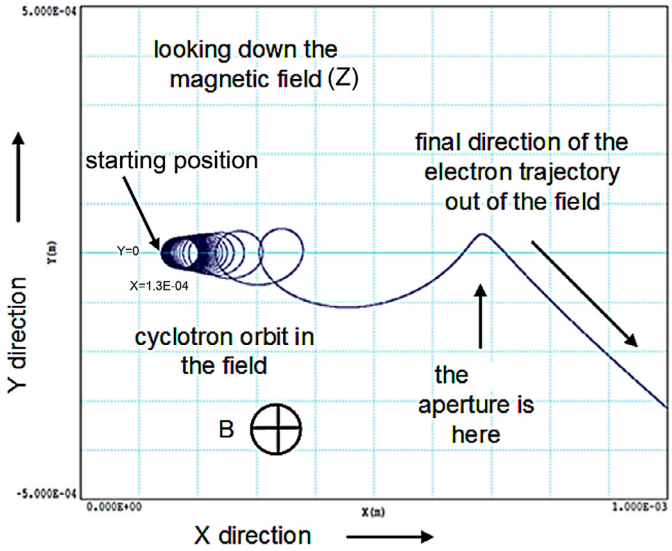

Figure 5. Simulated electron trajectory from an off-axis electron looking down the magnetic field.

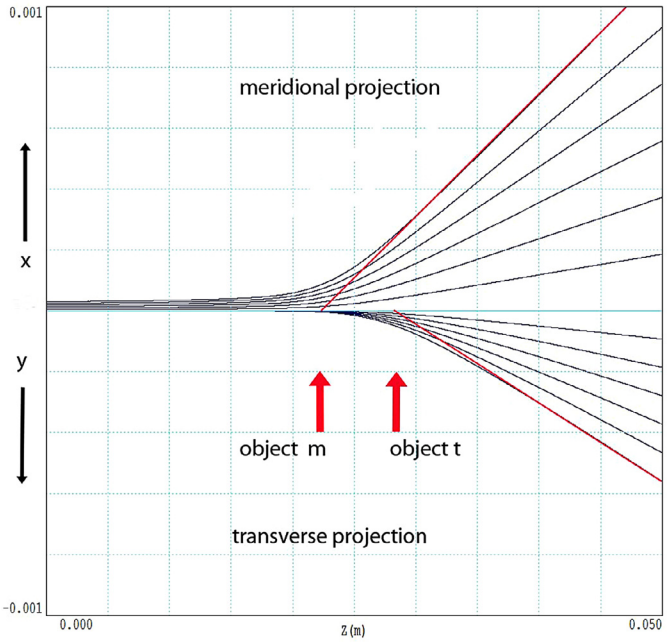

Figure 6. The apparent object positions in the meridional, and the transverse projections.

we can say that the angular magnification does go down with increased electron exit energy, but not quite with the inverse square law as we might expect. This is because the higher energy electrons leave the field lines at a different magnetic field to those at lower energy.

The size of the aperture also effects the magnification with a high field termination, but not with a low field termination. The shape of the aperture along the axis only has a small effect. Our conclusion is a choice of aperture size should be fixed on as appropriate to the size of the magnet in the region of several mm to a few centimeters in diameter. A larger aperture would be favored because the final part is required to be magnetically uniform. However again, if the magnet is small, the aperture will be small.

The ratio of the strength of the terminating magnetic field, and the strength of the central field is a choice that needs to be made with two aspects in mind. The first aspect is the angular magnification, and the second aspect is the field of view. The field of view not only depends on the angular magnification, but also on the real magnification of the sample size at the aperture. As the field of view from having a lower angular magnification gets larger, the increase in the size of the real image projected on the aperture gets larger. This reduces the size of the angular image that can be 'focused' into the CHA with the input lens. These factors are considered in the next section.

3. Rules of thumb for system design

We are interested in creating some rules of thumb for designing the VPPEM instrument in terms of the interaction between the field of view at the sample, and the energy resolution obtainable from a concentric hemispherical analyzer (CHA). As we have indicated in the introduction the image of the sample entering the CHA is not a simple angular image, it also has a spatial dimension. This spatial dimension is significant because there is a magnification of the field of view at the sample by the decrease in the magnetic field as the electrons move away from the strong central field. The angular image is also rotated with respect to the spatial image. Therefore, when we calculate the energy resolution when this image is projected by the input lens into the CHA, we have to

consider the combination of these image properties. To get a feel for this, we will combine those equations from the magnetic circuit, the input lens, and the CHA that approximately describe the image properties that we need.

The angular image size is determined by the angle made by the off-axis momentum gained from the vector potential field as the electron exits the magnetic field, and the forward momentum of the exiting electron.

$$\theta = \frac{p_a}{p_f} \tag{4}$$

Where the off-axis momentum is:

$$p_a = -e\boldsymbol{A} \tag{5}$$

And the forward momentum is:

$$p_f = \sqrt{2meE} \tag{6}$$

Where E is the energy of the electron in eV.

The vector potential **A** at radius r in a magnetic field **B** in Tesla will be:

$$\mathbf{A} = \frac{r\boldsymbol{B}}{2} \tag{7}$$

Combining these four equations gives:

$$\theta = k\frac{rB}{\sqrt{E}}\text{radians} \tag{8}$$

Where $k = 1.48\times10^5 = (0.125e/m)^{0.5}$.

The spatial magnification M of the magnetic field acting as a projection lens [5] depends on the square root of the ratio of the initial magnetic field at the sample B_s, and the final exit magnetic field B_e:

$$M = \sqrt{\frac{B_s}{B_e}} \tag{9}$$

If we have the maximum field of view at the sample as r_s, then we have the maximum angle in radians:

$$\theta_{max} = k\frac{r_s B_e}{\sqrt{E}}\sqrt{\frac{B_s}{B_e}} = k\frac{r_s\sqrt{B_e B_e}}{\sqrt{E}} \tag{10}$$

However, we know from our simulations (Supplemental file 2) that this is only approximately true for a very small aperture. For larger apertures this may be less than half of this.

The energy resolution of a CHA can be approximated by:

$$\frac{\Delta E}{E} = \frac{w}{2R} + \alpha^2 \tag{11}$$

Where w is the slit size, R is the center radius of the CHA, and α is the half angle of the electron entering the CHA.

To make a simplification we will make the CHA input lens an einzel lens, same input and output energy, with unity magnification.

Assuming the magnified field of view, $2r_s$, just fits into the CHA entrance slit w, and combining equations 9, 10, and 11, and adding a compensation factor of $(0.5)^2$ for the reduction in angle for a medium sized aperture (Supplemental file 2):

$$\frac{\Delta E}{E} = \frac{2r_s}{2R}\sqrt{\frac{B_s}{B_e}} + 0.25k^2r_s^2\frac{B_s B_e}{E} \tag{12}$$

Multiplying both sides by E:

$$\Delta E = \frac{r_s}{R}E\sqrt{\frac{B_s}{B_e}} + 0.25k^2r_s^2 B_s B_e \tag{13}$$

From equation 13 we have the balance between the lower magnetic field at the termination giving a lower angle, and the lower magnetic field at the termination giving a higher apparent image size. It can also be seen that for a fixed energy window the field of view is partly dependent on the size of the CHA. A larger CHA leads to a larger field of view. We can differentiate equation 13 with respect to the termination field to find the optimum termination field for any input assumptions.

$$B_e = \left(\frac{4E}{r_s k^2 R\sqrt{B_s}}\right)^{2/3} \tag{14}$$

We would like to have an energy resolution of better than 0.1 eV. We are not using the CHA primarily as a high quality spectrometer but we would like to sample takeoff energies below 1.0 eV to get better spatial resolution. Putting in some numbers into equations 13 and 14 for a 2.0 T and a 10.0 T field at the sample, and using a 150 mm radius CHA with a 50.0 eV pass energy.

At 2.0 T: With a complete field of view of 10 microns, we get an optimum final field from Equation 14 of 4.2E-2 T:

$$\Delta E = 1.7\text{E}-2$$
$$= 1.5\text{E}-2 + 2.3\text{E}-4 \qquad \alpha = 1.5\text{E}-2$$

At 10.0 T: With a complete field of view of 5 microns, we get an optimum final field from Equation 14 of 3.9E-2 T:

$$\Delta E = 1.3\text{E}-2$$
$$= 1.3\text{E}-2 + 2.6\text{E}-4 \qquad \alpha = 1.6\text{E}-2$$

These figures are only a guide as we have shown (Supplemental file 2) the equations do not scale as simply as we would like. However, this gives us a starting place in designing the electron optics. As a target for designing the magnetic circuit a final field in the region of several hundred Gauss can be used.

We can see our assumptions about the field of view also strongly influence our design. Because we do not have a fixed input slit to the CHA we do not have a fixed field of view. In fact, the imaging energy will have some dispersion across the final image. The field of view will be larger in the non-dispersive direction.

4. Simulation of Magnet, Input Lens, and CHA

The image properties are complex, and using Gaussian optics is not appropriate. To finalize a design, we need to simulate the magnet, the input lens, the CHA and the output lens together.

We have built two instruments, one with a liquid helium temperature magnet having a large $1.25\times1.25\times1.5$ meter independent ferromagnet shield [1], and another instrument with a compact $10\times10\times10$ cm HTS solenoid with a closely coupled electromagnetic yoke. The first instrument was a proof-of-principle, and even though it produced excellent results [2], we do not see this as the best model to follow. Instead, we will illustrate the process with the compact HTS approach.

The electron optical modeling was done using the Field Precision LLC 2D TriComp suite. The calculation of the trajectories through the optical path is broken into sections passing the output trajectories from one section as the input trajectories to the next. The magnetic and electric fields of the magnetic enclosure and the input lens are modeled as one unit because it was necessary to understand the effects of stray fields from the magnet on the input lens. The trajectories in the magnetic enclosure take significant computer time to process because the synchrotron orbits at low energies in a strong magnetic field need high precision. A large set of these trajectories are calculated, and used as inputs into the input lens which can be designed with less computational effort. To limit the range of the design parameters used for the input lens, a three element einzel lens with magnification of near unity was fixed on. The lens itself was adapted from the existing one on the CHA, and is a 4 element cylindrical electrostatic lens of 60 mm diameter and 450 mm length.

Figure 7 shows the complete magnetic enclosure and the CHA input lens as a sectional plot with magnetic and electrostatic fields shown as field lines. The section is rotationally symmetric around the horizontal axis.

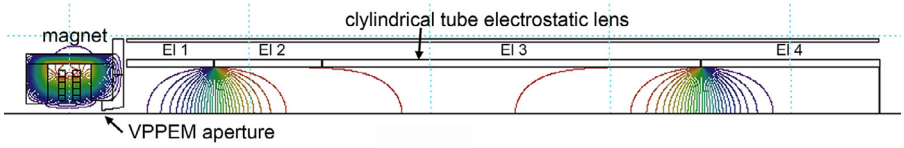

Figure 7. Magnetic and electrostatic fields for an HTS compact electromagnet and a CHA input lens operated as a 3 element einzel lens.

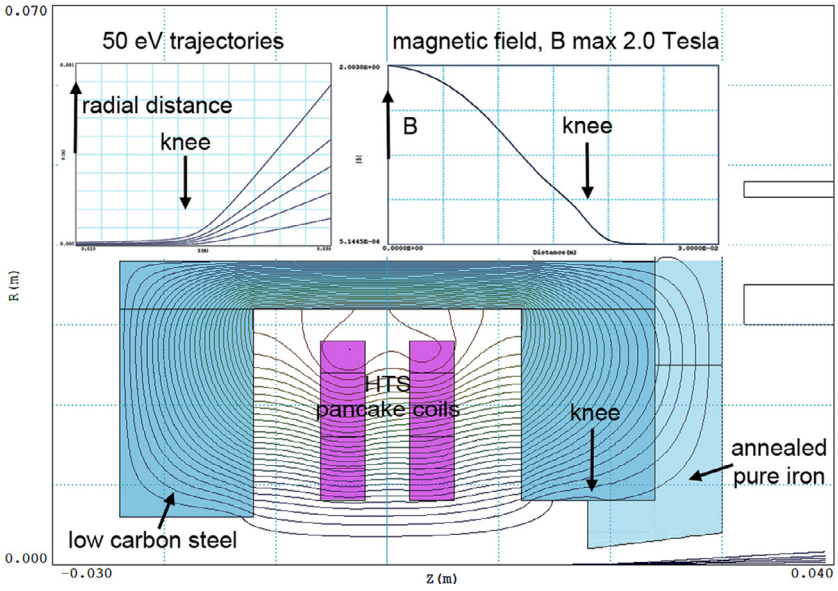

Figure 8. Simulation results for a compact HTS electromagnet. The maximum axial field is 2.0 Tesla. The iron aperture produces a knee in the decay of the field that causes the trajectories to leave the field lines at approximately 550 Gauss.

A simulation of the magnetic enclosure is shown in Figure 8. The magnetic circuit has an electromagnetic yoke making a significant contribution to the central field strength of 2.0 T. The mild steel yoke is 76 mm diameter, and 48 mm length. The 4 mm aperture insert is pure iron. Figure 8 upper right shows a plot of the decay of the central field. A distinct knee in the decay is created by the presence of the aperture. The 50 eV electron trajectories leave the field lines at approximately 550 Gauss which is slightly into the aperture. An expanded view of the trajectories is shown Figure 8 upper left.

Figure 9 shows the input lens with three illustrative 50 eV trajectories. The lens is operated as an accelerating three element einzel lens for 50 eV electrons with +490 V on the central element. There is also some focusing from the magnet's stray field penetrating into the lens. The 'focus' at the exit of the lens is actually a best fit to minimize the size. This best fit depends on the most extreme trajectory that will exit through the exit slit of the CHA. Trajectories though the CHA were

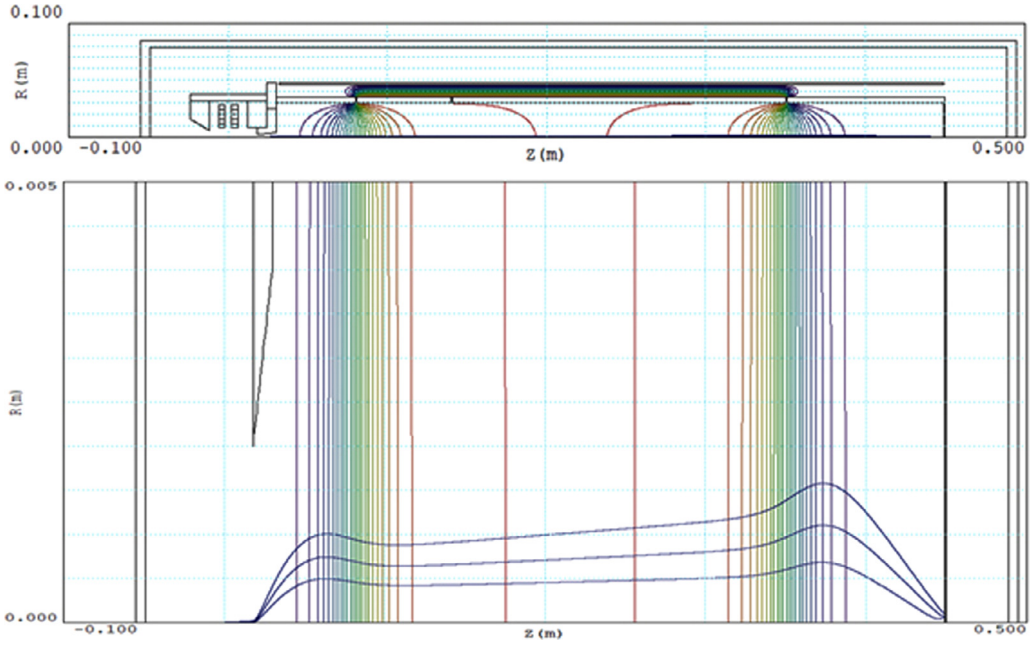

Figure 9. Illustrative input lens trajectories. Lower plot is an expanded view of the upper plot.

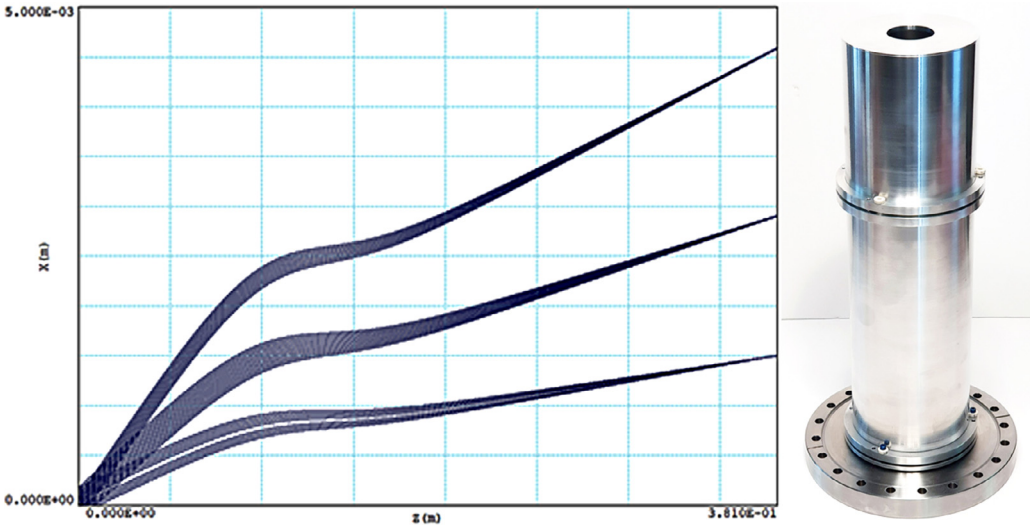

Figure 10. Output lens simulated trajectories with picture of uncoated lens assembly.

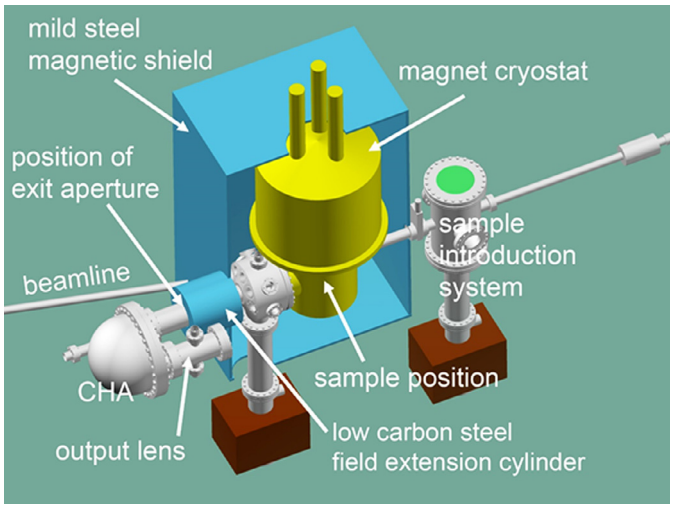

Figure 11. Schematic diagram showing the main parts of the VPPEM at NSLS U4A.

calculated using the CHA equation of motion [7].

$$\frac{x_o}{R} = -\frac{x_i}{R} + \frac{2\Delta E}{E} - 2\alpha^2 \tag{15}$$

Where R is the center radius of the CHA, α is the half angle of the electrons entering the CHA, and x_i and x_o are the distances of the incoming, and outgoing electron from the central radius R of the CHA. Using an Excel spread sheet, and the CHA equation of motion the final parameters of the input lens trajectories can be converted into the input trajectory parameters for the output lens. Only those trajectories that fall within the 0.35 mm output slit of the CHA are used.

The output lens takes the angular image from the CHA output slit, and focusses it onto an image plane. The optical equivalent is a simple lens with the object at infinity, and the real image at the focus. There is some curvature of the image plane, and chromatic aberration because there is energy dispersion across the image in the CHA energy dispersion direction. This suggests that we use a lens that is a large as possible help reduce image curvature.

The solution is simulated using trajectories output from the CHA as described above, Figure 10. In this case, the output lens is constrained by two geometrical factors. The first is that the CHA output port has an 8" CF flange, and the second is the length of the input lens which effectively limits the length of the output lens before it meets the magnet mounting. The lens focusses at 380 mm from the CHA output slit. The image detector is a 40 mm BOSS dual MCP with phosphor and an antireflection coated window mounted on a 6" CF flange. The simulation, and construction of the lens is straightforward.

To maximize the use of the 40 mm detector, we used a slightly higher exit field from the magnetic enclosure to give a factor x2 increase in angular magnification. This gives 500 lines per cm at the detector, and an estimated energy resolution of 50 mV. This compares with the 0.5 eV resolution of the proof-of-principle instrument at NSLS U4A.

6. Implementations

The proof-of-principle VPPEM was constructed at the National Synchrotron Light Source (NSLS) at Brookhaven National Laboratory [1]. The NSLS facility has now been superseded by NSLS II. The VPPEM was on beamline U4A which was an ultra-violet (20-90 eV) bending magnet beamline focused to a 2-3 mm spot size. The U4A spot size was comparatively large for microscopy with a low flux for monochromatic illumination with photons between 20-40 eV in the range of 5×10^3 photons/micron^2/s. Using monochromatic illumination with photons between 20-40 eV, images could be collected with 1-10 second exposure times.

Figure. 11 is a simplified rendering showing the main features of the equipment.

The VPPEM used a conventional liquid helium cooled superconducting solenoid. The solenoid sat at the center of a mild steel enclosure of 12 mm mild steel shield $1.25\times1.25\times1.5$ meter in size. The superconducting magnet was supported by a thin wall stainless steel inner chamber, and could not be expected to support any out-of-vertical forces. Necessarily, the magnetic circuit is of the type where there is a low interaction between the magnet and the shield. Forces on the magnet were balanced out by setting the magnet at the center of the shield. Residual forces were estimated to be less than 25 Newtons with a 1.8 Tesla central field.

A low carbon steel cylinder extended the field away from one side of the enclosure. The field exit aperture which sat at the end of the cylinder was made from an annealed soft iron ring with a 40 mm internal diameter. The magnetic field at the sample is 1.8 Tesla, and the photoelectrons exit the field at 1.5E-3 Tesla. There were also image steering coils within the steel cylinder. The intention of having this extension was to give room for the incoming beam and other experimental probes. However, in retrospect, this was not a good magnetic design

because the extension cylinder also projected stray fields. It was found necessary to have an external coil around the cylinder to reduce stray fields from this source.

The superconducting solenoid had an air bore that the microscope UHV vacuum chamber passed through. The sample was supported by a 24" long throw three axis stage at the center of the magnetic field. The sample was passed into the magnet from a sample preparation chamber at the back of the instrument. There were also X,Y coils inside the air bore at the sample position that could be used to move the center of the magnetic field, and therefore move the apparent sample position without physically moving the sample. The UHV chamber had a variety of ports to allow a beam line to illuminate the sample, and to view the sample position optically. The CHA used was a 100 mm diameter VLS instrument. The beam was incident at 15° to the axis of the magnet.

Several lessons came out of using the instrument. The first lesson is that a large magnetic field is very difficult to fully shield. A set of large bucking coils were needed to put the CHA and the imaging lens mu-metal shields into a low enough field to be effective. Another lesson was that vibration control needs a different approach compared to a normal microscope. Great care was taken to stiffen, and vibrationally isolate the optical bench that the magnet and the CHA sat on. Figure 12 shows the optical bench which was a thick Al plate attached to a pneumatic anti-vibration table. However, the critical area for vibration control is actually within the magnetic enclosure. Vibration of the sample within the magnetic field is the important factor. Moderate vibrations in the X,Y directions along the main optical path after the magnetic enclosure do not affect the image: firstly, because it is an angular image, secondly, there is image magnification inside the magnetic enclosure. A welcome surprise was that, even though the sample was mounted on a long throw manipulator using an 18 mm diameter Al rod, it was found that magnetic damping of the sample stage in the 1.8 tesla field meant that short period vibrations were effectively damped out. Long term drift was removed computationally. The lesson is that the stage needs to be made from aluminum or copper.

If we compare this design with our calculations of section 3 we can see that this is not an optimum design. For a 100 mm radius CHA, 1.8 T central field, and a 40 mm diameter exit aperture (where the compensation factor will be near 0.25) the optimum exit field would be several hundred Gauss compared to 15 Gauss of the actual instrument.

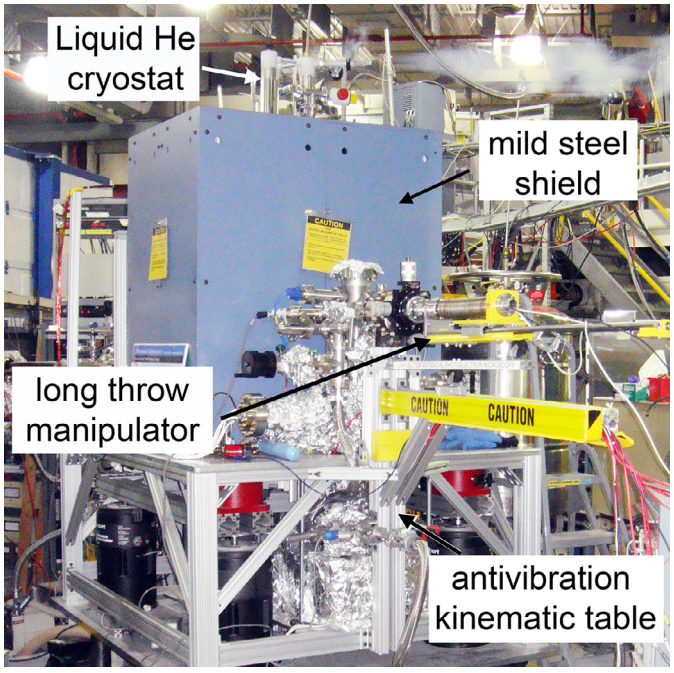

Figure 12. Back view of VPPEM proof-of-principle instrument.

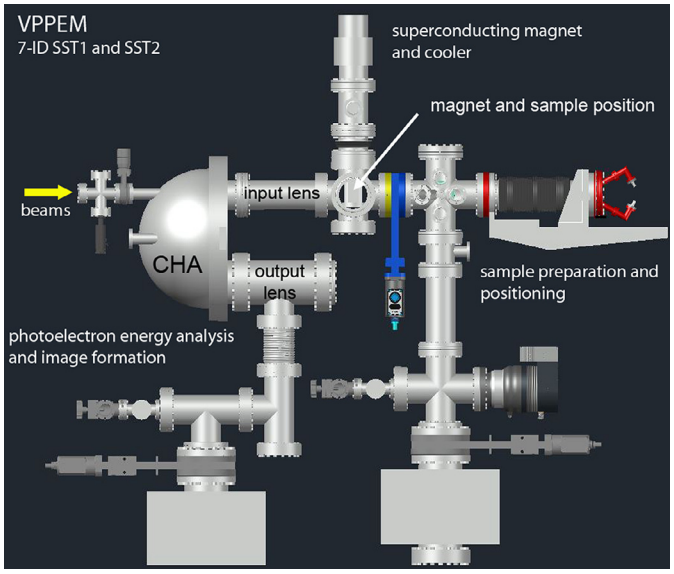

Figure 13. CAD rendering of VPPEM instrument at NSLS II 7-ID.

The result of this was that the energy resolution was low, approximately 0.5 eV, and there was a 1.0-2.0 eV energy dispersion across the image of 75 microns.

Despite the limitations in this first instrument design, and the low photon flux, useful results were obtained [2, 8]. These results demonstrated that the VPPEM technique has significant potential as an analytical technique. The lessons learned have been used to construct a second instrument on the NIST high brightness beamlines at NSLS II using the electron optical design in section IV. A CAD rendering of this instrument is shown in Figure 13.

In this new implementation at NSLS II, there is an added design complication in that the instrument is the endstation of two beamlines [9]. This required that two extra ports to be cut through the CHA, which is a 150 mm radius instrument. The two beamlines on NSLS II 7-ID are high brightness undulator beamlines: SST1 80 eV- 2,000 eV and SST2 2.0 KeV - 7.5 Kev. The beamlines are angled at 6.6° in the horizontal plane. Given the angle of the dual ports and apertures through the CHA, there are additional geometrical constraints placed on the magnet size and position at the intersection of the beamlines. A compact well shielded magnet is a necessity because it cannot be stood back from the CHA and the input lens. We have used an HTS approach with a compact shielded electromagnet constructed inhouse. The magnet uses a dual HTS pancake winding with only 70 meters of tape. A 4 mm diameter aperture in a 99.99% iron insert into the steel yoke with a careful softening anneal is used for the field termination. The dual HTS pancake coils and the magnet is shown in Figure 14. Simulation of this magnet is shown in Figure 8.

Figure 15 shows at complete microscope at NSLS II 7-ID. The sample

Figure 14. A 2T shielded dual pancake coil HTS magnet with a soft iron aperture insert.

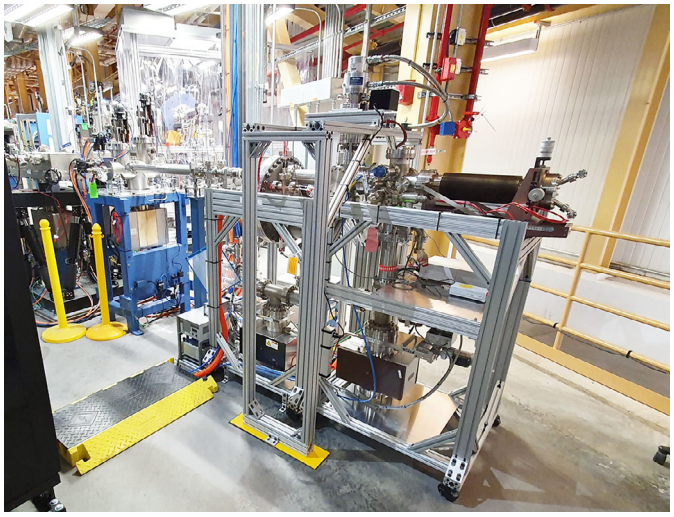

Figure 15. Second generation VPPEM at the NSLS II 7ID SST1 and SST2 endstation.

is supported on a long throw manipulator which passes from the sample preparation chamber into the magnet from the back. The main parts of the microscope and its pumping stacks are supported on an extruded Al frame without the antivibration table of the proof-of-principle instrument.

7. Definition of the angular image, notes on the VPPEM and PEEM electron optics

The angular image exiting from the VPPEM magnetic field aperture is an unusual type of image, only a field emission microscope (FEM) could be considered to have a similar form [10]. In our context, we define the term angular image in that the two-dimensional (X,Y) spatial information from the sample is encoded as a mapping onto a two-dimensional angular distribution. The two dimensions being: θ the off-axis angle or inclination, and φ the azimuthal direction around the optical axis. The angular image coming out of the magnetic field aperture can be seen as the electron optical equivalent of the image within a pinhole camera. Each ray from a different point of an object comes through the pinhole at a different angle, and is then projected onto a screen. A phosphor screen placed in front of the magnetic field aperture would provide a similarly projected image if the electrons were monochromatic.

The fact that the signal is encoded as an angle after leaving the magnetic field has a large impact on the design of the electrostatic section of the electron optics. We illustrate this below in a comparison with the electron optics of the cathode lens class of photoelectron emission microscope, PEEM.

Although we are ultimately using the angular information, as we have discussed in Section 1, the image coming out of the field aperture is actually a mixture of spatial, and angular information. The result is that the CHA input lens does not really 'focus' into the CHA. The input lens produces a non-Gaussian somewhat caustic looking focus. However, these apparent aberrations are in space not in angle. Similarly, for the intrinsic chromatic aberration of the CHA. The CHA is double focusing in θ and φ, however, the energy-dispersed image at the exit of the CHA is not like the original pinhole image but is spread out across the CHA output aperture in the dispersion direction. We can still form a good image with the CHA output lens because we are focusing on an angular image which is a virtual image at infinity. The output lens is a telescope with the detector at the prime focus.

In contrast, PEEM that includes energy spectroscopy must somehow compensate for the energy analyzer chromatic aberration on the real image. This is done in one of two ways, either to move the real image back away from the CHA, and use a virtual image through the CHA [11], or to use a double CHA to compensate for the image shift [12, 13]. Both approaches are complex in the electron optical design and implementation. One issue is that the cathode lens microscope uses a large accelerating voltage to form the image. A design is required to use electrostatic decelerating lenses to inject the image into the CHA. This is because the CHA requires a relatively low pass energy to give sufficient energy resolution. Decelerating lenses do two things, one is to increase the angle of the image, and thus increase aperture size, and second, electrostatic decelerating lens are very aberrating. The full solution to this problem is a remarkable series of instruments PSMART PEEM /LEEM BESSY [14-16], and NanoESCA [12, 13, 17]. However, these instruments are significantly more complex than the design shown in this report. Using an angular image at low voltage gives us the advantage of simplicity in the design of the electron optics.

From a consideration of the electron optics, and the mechanism of image formation, it can be seen that VPPEM does not lend itself naturally to many of the important measurements that are the main elements of PEEM investigations [18]. For example, the collimating action of the magnetic field rules out measurement of the k-vector [19], and because of the saturating effect of the magnetic field we cannot expect to see any useful information using magnetic dichroism [20, 21]. Also, as we have designed in a near normal incidence for the photons onto the sample, using the polarization of the photons to look at surface electron orbital orientation [22] would require a large sample tilt.

We are using partial yield NEXAFS as the primary imaging signal. For this the main task of the spectrometer is to discriminate low energy electrons in the range 0f 0.5-1.5 eV to maximize the spatial resolution. However, with a 50 mV energy resolution we should also be able to image surface potentials using a series of images scanning the sample voltage over the range of a few volts. We can also image the directly emitted photon electron which in principle can give us some form of depth profiling by changing the detected emission energy, and thus the escape depth in the solid. We have done a very preliminary demonstration of this [8].

We should note that there are many aspects of the VPEEM optics that have not been fully explored experimentally. These include space charge, sample charging issues, sample voltage differences, topographic effects, and sample related spatial resolution. VPPEM will not be susceptible to image degradation due to space charge effects [14] for although it has in effect a 'back plane' crossover of the image at the CHA entrance, this is not a true crossover. This crossover has a both spatial and angular size. PEEMs have a contrast aperture in the focal back plane to restrict the energy and angular spread of electrons, allowing tradeoff between resolution and transmission. This crossover does introduce the problem of space charge that ultimately degrades the image for high brightness synchrotron photon sources. There is no such angle limiting mechanism for the VPPEM. Electrons leaving the surface at all angles are constrained to travel down the magnetic field lines, and are then collimated as the field decays. Sample charging will not effect VPPEM in the same way that it does PEEM [23]. Sample surface topography effects which are strong with PEEM [24] are relatively insignificant with VPPEM. This is partly because of the large depth of focus, but also because the surface is not immersed in a strong electrostatic field. One currently unresolved issue is the effect of sample properties on the spatial resolution. The calculated special resolution is determined by the electron energy and the magnetic field. From equation 3, for a 1 eV electron energy and a 2 Tesla field we expect a 20-80% resolution of 1.5 micron. However, we observe much higher resolutions on some samples [2], and this is still not understood.

Looking at the electron optics, we expect that VPPEM will have a place in the analysis of engineering materials which are not flat planes, good conductors, or even consolidated samples such as powder residues. The electron optics of VPPEM and PEEM have very different imaging properties, they can be seen as interestingly similar, but ultimately non-competing techniques.

8. Conclusion

There is a great deal of flexibility in the design of a VPPEM instrument. We have set out some rules of thumb for designing a VPPEM. However, we can expect that there would be a wide variation in any new implementation. Lessons from the proof-of-principle VPPEM have been incorporated into the second generation instrument at NSLS II. The elements that comprise a VPPEM are not overly specialized, and it is possible that construction of a useful instrument can be achieved with limited modifications of existing parts.

Acknowledgments

My thanks to Daniel Fischer of NIST for his support of this work. This work has been supported under NIST SBIR contract 1333ND19CNB640027. This research used resources of the National Synchrotron Light Source, a U.S. Department of Energy (DOE) Office of Science User Facility operated for the DOE Office of Science by Brookhaven National Laboratory under Contract No. DE-AC02-98CH10886, and of the National Synchrotron Light Source II under Contract No. DE-SC0012704.

Supplementary materials

Supplementary material associated with this article can be found, in the online version, at doi:10.1016/j.ultramic.2020.113022.

References

[1] R. Browning, Vector potential photoelectron microscopy, Review of Scientific Instruments 82 (10) (2011) 103703, , https://doi.org/10.1063/1.3648135.
[2] Browning, R., Enhanced spatial resolution in vector potential photoelectron microscopy. 2017.267(2): p. 176-192. DOI: doi:10.1111/jmi.12558.
[3] R. Browning, J. Woicik (Ed.), Editor, Springer International Publishing: Cham, 2016, pp. 533–554, , https://doi.org/10.1007/978-3-319-24043-5_19.
[4] P Richard., R.B.L. Feynman, Matthew Sands The Feynman Lectures on Physics: Mainly Electromagnetism and Matter 2 Addison-Wesley, 1964.
[5] G. Beamson, H.Q. Porter, D.W. Turner, The collimating and magnifying properties of a superconducting field photoelectron spectrometer, Journal of Physics E: Scientific Instruments 13 (1) (1980) 64–66, https://doi.org/10.1088/0022-3735/13/1/018.
[6] Browning, R., Spatial resolution in vector potential photoelectron microscopy. 2014.85(3): p. 033705. DOI: 10.1063/1.4868559.
[7] C.E. Kuyatt, J.A. Simpson, Electron Monochromator Design, Review of Scientific Instruments 38 (1) (1967) 103–111, https://doi.org/10.1063/1.1720492.
[8] R. Browning, NEXAFS/XPS spectra, and information depth using low energy electron spectromicroscopy in a VPPEM, Journal of Electron Spectroscopy and Related Phenomena 195 (2014) 125–131, https://doi.org/10.1016/j.elspec.2014.06.005.
[9] R. Reininger, et al., NIST NSLS-II spectroscopy beamline optical plan for soft and tender X-ray spectroscopy and microscopy (100eV to 7.5keV). Nuclear Instruments and Methods in Physics Research Section A: Accelerators, Spectrometers, Detectors and Associated Equipment 649 (1) (2011) 49–51, https://doi.org/10.1016/j.nima.2010.11.172.
[10] E.W. Müller, Das Feldionenmikroskop, Zeitschrift für Physik 131 (1) (1951) 136–142, https://doi.org/10.1007/BF01329651.
[11] B.P. Tonner, et al., A photoemission microscope with a hemispherical capacitor energy filter, Journal of Electron Spectroscopy and Related Phenomena 84 (1) (1997) 211–229, https://doi.org/10.1016/S0368-2048(97)00005-4.
[12] M. Escher, et al., Nanoelectron spectroscopy for chemical analysis: a novel energy filter for imaging x-ray photoemission spectroscopy, Journal of Physics: Condensed Matter 17 (16) (2005) S1329–S1338, https://doi.org/10.1088/0953-8984/17/16/004.
[13] M. Escher, et al., Applications of high lateral and energy resolution imaging XPS with a double hemispherical analyser based spectromicroscope, Journal of Electron Spectroscopy and Related Phenomena (2010) 178–179, https://doi.org/10.1016/j.elspec.2009.06.001 303-316.
[14] T. Schmidt, et al., First experimental proof for aberration correction in XPEEM: Resolution, transmission enhancement, and limitation by space charge effects, Ultramicroscopy 126 (2013) 23–32, https://doi.org/10.1016/j.ultramic.2012.11.004.
[15] T. SCHMIDT, et al., XPEEM WITH ENERGY-FILTERING: ADVANTAGES AND FIRST RESULTS FROM THE SMART PROJECT, Surface Review and Letters 09 (01) (2002) 223–232, https://doi.org/10.1142/s0218625x02001811.
[16] S.L. Christensen, et al., Partial secondary electron-yield NEXAFS spectromicroscopy with an energy-filtered X-PEEM, IBM Journal of Research and Development 55 (4) (2011) 1–5, https://doi.org/10.1147/JRD.2011.2143550 56.
[17] A. Bailly, et al., Aspects of lateral resolution in energy-filtered core level photoelectron emission microscopy, Journal of Physics: Condensed Matter 21 (31) (2009) 314002, , https://doi.org/10.1088/0953-8984/21/31/314002.
[18] E. Bauer, LEEM, SPLEEM and SPELEEM, Springer International Publishing, 2019, https://doi.org/10.1007/978-3-030-00069-1_9 2-2.
[19] T.O. Menteş, A. Locatelli, Angle-resolved X-ray photoemission electron microscopy, Journal of Electron Spectroscopy and Related Phenomena 185 (10) (2012) 323–329, https://doi.org/10.1016/j.elspec.2012.07.007.
[20] G. Schönhense, Imaging of magnetic structures by photoemission electron microscopy, Journal of Physics: Condensed Matter 11 (48) (1999) 9517–9547, https://doi.org/10.1088/0953-8984/11/48/311.
[21] A. Locatelli, E. Bauer, Recent advances in chemical and magnetic imaging of surfaces and interfaces by XPEEM, Journal of Physics: Condensed Matter 20 (9) (2008), https://doi.org/10.1088/0953-8984/20/9/093002 093002.
[22] J. Stöhr, D.A. Outka, Determination of molecular orientations on surfaces from the angular dependence of near-edge x-ray-absorption fine-structure spectra, Physical Review B 36 (15) (1987) 7891–7905, https://doi.org/10.1103/PhysRevB.36.7891.
[23] B. Gilbert, et al., Charging phenomena in PEEM imaging and spectroscopy, Ultramicroscopy 83 (1) (2000) 129–139, https://doi.org/10.1016/S0304-3991(99)00196-5.
[24] S.A. Nepijko, et al., Resolution deterioration in emission electron microscopy due to object roughness, Annalen der Physik 9 (6) (2000) 441-451 10.1002/1521-3889(200006)9:6<441::AID-ANDP441>3.0.CO;2-J.